Available online at www.sciencedirect.com

ScienceDirect

journal homepage: www.elsevier.com/locate/he

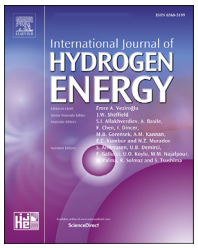

Hydrogen-assisted cracking of GMA welded 960 MPa grade high-strength steels

Thomas Schaupp [a,*], *Wolfgang Ernst* [b], *Helmut Spindler* [b], *Thomas Kannengiesser* [a,c]

[a] *Bundesanstalt für Materialforschung und -prüfung (BAM), Division 9.4 - Weld Mechanics, Unter den Eichen 87, 12205 Berlin, Germany*

[b] *Voestalpine Stahl GmbH, Voestalpine-Straße 3, 4031 Linz, Austria*

[c] *Otto von Guericke University of Magdeburg, Institute of Materials and Joining Technology (IWF), Universitätsplatz 2, 39106 Magdeburg, Germany*

HIGHLIGHTS

- Hydrogen-assisted cracking (HAC) of steels S960QL and S960MC is studied.
- Hardness in heat-affected zone (HAZ) of S960QL is significantly increased.
- Embrittlement index (EI) is 0.30 for the S960QL and 0.46 for the S960MC.
- Fracture topography of S960MC shows a low degree of degradation.
- HAZ of S960MC shows better resistance to HAC compared to HAZ of S960QL.

ARTICLE INFO

Article history:
Received 9 April 2020
Received in revised form
6 May 2020
Accepted 8 May 2020
Available online 6 June 2020

Keywords:
High-strength steel
Welding
Diffusible hydrogen
Hydrogen-assisted cracking
Heat-affected zone
Implant test

ABSTRACT

High-strength steels with yield strength of 960 MPa are susceptible to hydrogen-assisted cracking (HAC) during welding processing. In the present paper, the implant test is used to study HAC in a quenched and tempered steel S960QL and a high-strength steel produced by thermo-mechanical controlled process S960MC. Welding is performed using the gas-metal arc welding process. Furthermore, diffusible hydrogen concentration (H_D) in arc weld metal is determined. Based on the implant test results, lower critical stress (LCS) for complete fracture, critical implant stress (σ_{krit}) for crack initiation, and embrittlement index (EI) are determined. At H_D of 1.66 ml/100 g, LCS is 605 MPa and 817 MPa for S960QL and S960MC, respectively. EI is 0.30 and 0.46 for S960QL and S960MC, respectively. Fracture surfaces of S960QL show higher degradation with reduced deformation. Both, higher EI of S960MC and fractography show better resistance to HAC in the HAZ of S960MC compared to S960QL.

* Corresponding author
E-mail address: thomas.schaupp@bam.de (T. Schaupp).

https://doi.org/10.1016/j.ijhydene.2020.05.077

Introduction

Current efforts in lightweight design of steel constructions as well as the required reduction of CO_2 emissions and the increase in energy and resource efficiency require the use of high-strength steels. In building, plant and crane construction, for example, steels with yield strengths of 690 MPa–1100 MPa are mainly used [1,2]. In recent years, steels with yield strength of 1300 MPa have been developed [3]. Focus in the use of high-strength steels is the maximization of load capacities with low tare weight and a remarkable reduction of welding costs. Joining of high-strength steels by welding is primarily carried out using the gas-metal arc welding (GMAW) process. Filler materials with a nominal yield strength of up to 930 MPa are currently available for this purpose [4]. Current research is concerned with the development of filler materials with a yield strength of up to 1100 MPa [5,6].

Even though high-strength steels are considered to have good weldability, the requirements for the welding processing are becoming much more stringent with increasing strength. Due to the martensitic and bainitic microstructure, narrow process limits must be maintained to ensure the mechanical properties in the welded joint. Especially, the risk of hydrogen embrittlement can increase for high-strength steels with yield strength $\geq$ 960 MPa. During welding, hydrogen-assisted cracking (HAC) can result from a local critical combination of diffusible hydrogen, mechanical stress/strain and crack-critical microstructure in the heat-affected zone (HAZ) or in the weld metal [7]. A variety of theories on HAC can be found in the literature. A general overview about the mechanisms is given in a review paper by Lynch [8]. Djukic et al. [9] describe the interplay of most common mechanisms localized plasticity and decohesion. All theories have a degradation of the mechanical properties in the presence of hydrogen in common. Rhode et al. [10] investigated the effect of diffusible hydrogen on mechanical properties such as strength and elongation or reduction of area. For this purpose, tensile samples were electrochemically charged with hydrogen. It was found that hydrogen influences the deformability rather than the strength. Zimmer et al. [11] also demonstrated an increase in degradation with increasing strength of high-strength steels in presence of hydrogen. Villalobos et al. [12] investigated the degradation of modern micro-alloyed steels as a function of tempering temperature. In this case, as well, a significant decrease of elongation is reported. It is therefore important to keep the amount of diffusible hydrogen to a minimum when welding such materials. The main sources of hydrogen in welding are the filler material, moisture in the atmosphere or impurity on the material's surface. Particularly, inappropriate storage and handling of filler materials can have a significant negative effect on the performance of welded joints as reported by Pandey et al. [13]. Apart from that, hydrogen uptake during welding can be controlled by welding parameters, welding process and the type of filler material [14–16]. The diffusible hydrogen concentration can be reduced by a proper choice of the process parameters and the layer build-up during welding. However, complete hydrogen effusion out of the weld metal is only achieved by dehydrogenation heat treatment after welding [17]. The mechanical stresses are largely defined by the design of the construction as well as by the process parameters and can only be influenced to a limited extent [18]. The proper choice of base and filler materials should therefore be considered during the design phase of steel constructions to reduce the HAC formation to a minimum.

Particular attention is required for the HAZ of the base materials regarding HAC, since the thermal cycle during welding can cause a decrease in toughness depending on the used material and an increase in hardness and grain coarsening at peak temperatures above 1200 °C. This in turn can lead to a very susceptible microstructure to HAC [7]. In particular, the established quenched and tempered (QT) high-strength steels form a martensitic coarse-grained HAZ (CGHAZ) with high hardness. The reason for this is the high carbon content of 0.14 wt.-% to 0.21 wt.-% [1]. The addition of micro-alloying element Nb promotes the formation of Nb (C, N) type precipitates which improves grain refinement and toughness in the production of QT steels [2]. However, these precipitates can dissolve during welding at very high temperatures in the CGHAZ. Whereas in some materials a post weld heat treatment (PWHT) leads to a decrease of hardness gradient and thus to a less susceptible microstructure to HAC [19], PWHT is not considered after GMA welding of high-strength structural steels. Nevertheless, in order to reduce the hardening in the HAZ, high-strength steels produced by thermo-mechanical controlled process (TMCP) with controlled cooling have been developed [20,21]. The reduced carbon contents in the range of 0.03 wt.-% to 0.17 wt.-% result in an improved weldability compared to QT steels. Moreover, these steels have a higher proportion of micro-alloying elements (Nb, Ti, V). The formation of carbides and nitrides is then used to achieve grain refining effects and precipitation hardening. Due to the high temperature stability, Ti-rich nitrides cause a smaller grain size in the CGHAZ [22,23]. In combination with the lower carbon content, a softer and fine-grained microstructure in the HAZ is the result in case of TMCP steels [24,25]. According to Graville [26], the carbon content and alloying composition (in terms of carbon equivalent CE) correlates with the susceptibility to HAC in the HAZ. This means that weldability gets more difficult with increasing carbon content and CE. The risk of HAC formation is therefore increased.

The diffusion of hydrogen in high-strength steels is directly related to microstructure. The diffusivity of hydrogen in steels decreases with increasing alloying content [27,28]. Mainly precipitates and grain boundaries play an important role. Steppan et al. [29] investigated the trapping behavior in physically simulated weld structures of 690 MPa grade QT and TMCP steels. The CGHAZ of QT steel had a prior austenite grain size of 106 μm, which was higher than that of TMCP steel (57 μm). In addition, the CGHAZ of the TMCP steel showed a higher hydrogen solubility and an increased trapping behavior. For the QT steel, mainly dislocations and Cr-rich carbides were identified as hydrogen traps, whereas for the TMCP steel, primarily grain boundaries and Ti-rich carbides and nitrides were defined as reasons for trapping. An increase of hydrogen trapping with decreased grain size is also reported in Ref. [30–32]. Accordingly, it can be assumed that the

mobile hydrogen content in the TMCP steel's HAZ can be lowered and thus the susceptibility to HAC is reduced.

Many test methods exist for the investigation of HAC for high-strength steels [33,34]. These tests provide qualitative (crack/no crack) or quantitative (critical stress levels) results depending on the materials combination and test parameters. In principle, the test methods for HAC can be divided into self-restraint and externally loaded tests. In the case of the self-restraint tests, the mechanical stresses are produced purely by the global and local residual stresses resulting from the restraint of shrinkage and the phase transformation in the weld area associated with a change in volume. In the case of externally loaded tests, the mechanical stress is applied by a suitable loading device. However, the residual stresses are not considered in the evaluation. The implant test is the most common externally loaded cold cracking test method, which was developed by Henry Granjon in 1969 [35]. The main feature of this test method is the user-defined tensile load on a representative material volume of the tested material directly at the weld seam and can be used for quantitative investigations of HAC susceptibility of the HAZ. HAC in the weld metal is hardly considered. Furthermore, a transfer of the results to welded components is only possible to a limited extend, since no joint welds are carried out in the implant test. Therefore, the cracking behavior does not correspond to the real case. But it allows a material ranking. The implant test was used to study delayed cracking [36,37] as well as the influence of diffusible hydrogen concentration [38,39], heat input [40] and different types of base and filler materials [41–43] on the critical stress for crack initiation. Current research has focused on the influence of microstructure in the HAZ on the cracking behavior [44–46]. Comparisons of QT and TMCP steels were carried out.

Yue et al. [44,45] used the implant test to compare the HAC susceptibility in the HAZ of a QT and TMCP steel with a nominal yield strength of 690 MPa. The results showed higher critical stress levels for crack initiation with a significantly lower hardness in the CGHAZ in case of TMCP steel. This was attributed to the low carbon content and smaller grain size in case of the TMCP steel. The topography of the fracture surface of the implant samples showed a high deformability in the case of TMCP steel. This topography showed no change with variation of the hydrogen content. Kang et al. [46] achieved similar results via implant tests on steels with yield strength below 500 MPa. This is in good agreement with the results of Steppan et al. [29]. The TMCP steel seems to have a higher solubility and trapping behavior for hydrogen, which does not directly participate in HAC formation in the HAZ. Consequently, the TMCP steel has a better resistance to HAC in the HAZ. However, investigations on steels with higher strengths do not exist so far.

Therefore, the aim of the present study is to determine the HAC susceptibility in the HAZ of high-strength steels with a yield strength of 960 MPa as a function of microstructure, see Fig. 1. For this purpose, an QT steel was compared to a TMCP steel in order to show the influence of the chemical composition or the manufacturing process to HAC. For this purpose, the implant test was used to determine critical stress values for crack formation at constant hydrogen levels and same loading scenarios. This test was accompanied by ISO 3690 [47]

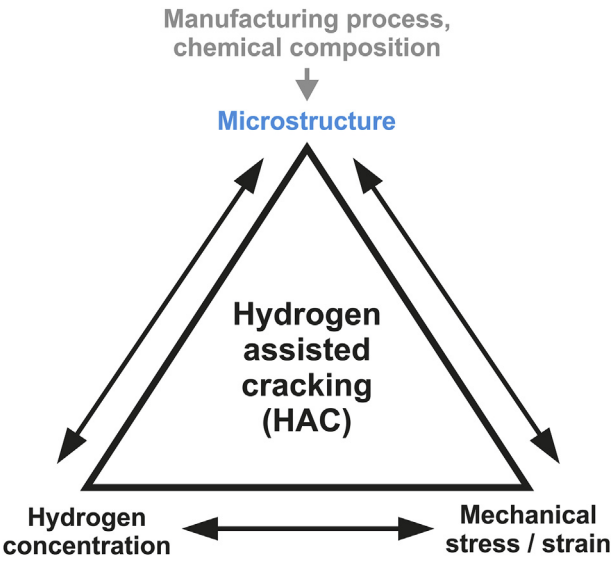

Fig. 1 – Influence of local factors on HAC susceptibility in the HAZ.

specimens and carrier gas hot extraction (CGHE) technique to determine the hydrogen concentration in arc weld metal. Examinations by light optical microscopy (LOM) and hardness testing were used to analyze the microstructure in the CGHAZ. In addition, investigations using scanning electron microscopy (SEM) were used for fracture surface analyses.

Experimental work

Test materials

For the investigations the high-strength steels S960QL (EN 10025–6 [48]) and S960MC (EN 10149–2 [49]) were used in the form of 8 mm rolled plates. The S960QL was produced by the conventional QT process [1,2]. The hot rolling process above recrystallization temperature is followed by cooling in air and then by a two-stage quenching and tempering process. The plates are heated above Ac_3, followed by quenching in water, which permits microstructural transformation in the bainite or martensite stage. The martensitic microstructure produces a high hardness due to the carbon content. Final tempering process in the temperature range from 500 °C to 600 °C reduces the hardness and improves the toughness [1,20]. In addition, alloying with Nb improves toughness of tempered martensite [2]. For comparison, the TMCP steel S960MC was used [20]. Thermo-mechanical rolling above Ac_3 produces in combination with micro-alloying elements (Ti, Nb, V) a very fine-grained microstructure with very good relation between strength and toughness. The austenite is deformed while recrystallization is hindered leading to an increased number of nuclei for transformation. A following direct accelerated cooling and tempering leads to a microstructure consisting of mainly tempered martensite. The filler material (FM) used was the high-strength solid wire G 89 5 M Mn4Ni2.5CrMo according to ISO 16834-A [50] (AWS A5.28: ER120S-G) with a diameter of 1.2 mm and a nominal yield strength of 930 MPa. The chemical

composition of the test materials is shown in Table 1. The mechanical properties are listed in Table 2.

When comparing the chemical composition of the base materials in Table 1, the lower carbon content (0.09% C) and the higher CE of S960MC are noticeable compared to S960QL (0.17% C). According to Graville [26,51] the S960MC is in Zone I in Fig. 2 which indicates a low susceptibility to HAC in the HAZ. S960QL with a higher carbon content and a relatively high CE is in Zone III with a HAC susceptible microstructure in the HAZ under all welding conditions. Yue et al. [44,45] already demonstrated the applicability of the Graville diagram to modern 690 MPa grade high-strength steels by using the implant test.

Implant test

The HAC susceptibility in the HAZ of the base materials from Tables 1 and 2 was studied by using the implant test according to ISO 17642–3 [53]. Fig. 3 shows schematically the implant test. For the tests, the implant specimen with a spiral notch and a diameter of 6 mm was inserted into the hole of an unalloyed structural steel plate (200 mm × 300 mm × 20 mm). The bottom end of the implant specimen was fixed with a load cell of the loading device. As the implant specimens had to be fixed by means of M10 threads, but the sheets of the base materials only had a thickness of 8 mm, build-up welding was carried out using the FM (Table 1). The threads were then produced on this build-up welds, see Fig. 3(a). Before welding all surfaces were cleaned with acetone. The specimen plate and implant specimen were then joined by a bead-on-plate weld using the GMAW process and the welding parameters from Table 3 without pre-heating. The used shielding gas was ISO 14175-M21-ArC-18 with a gas flow of 18 l/min. To determine the cooling times type-K-thermocouples with a diameter of 0.8 mm were plunged into the molten pool during welding. The $t_{8/5}$-time (time difference during cooling between 800 °C and 500 °C) was used to describe the microstructure. The $t_{3/1}$-time (time difference during cooling between 300 °C and 100 °C) served as a parameter for the stability of the welding process and the heat transfer in the samples. Immediately after cooling to a temperature of 150 °C, the implant specimens were subjected to a defined static tensile load according to the standard [53]. The time to failure (TTF) of the implant specimen was registered as a function of the applied stress. The maximum loading duration was 24 h, while the standard recommends 16 h. The aim was to enable a qualitative estimation (fracture or no fracture) and the quantitative determination of the maximum stress for avoiding cracking.

The maximum stress at which no fracture occurred after 24 h of loading was called "lower critical stress" (LCS), which also was used by other authors to evaluate the HAC susceptibility [38,43–45]. However, in these investigations the implant geometry according to the AWS standard [54] was used, which is different from the geometry of the ISO standard [53]. When using the ISO geometry, incipient cracks can occur at applied stresses below LCS in unfractured specimens. Therefore, the "critical implant stress" σ_{crit} was introduced in addition to the LCS in order to use the incipient cracks as an evaluation criterion.

Table 2 – Mechanical properties of test materials.

Material	Yield strength $R_{p0.2}$ in MPa	Tensile strength R_m in MPa
S960MC[(a)]	1019	1026
S960QL[(a)]	964	1047
FM[(b)]	≥930	≥980

(a) Mechanical testing.
(b) According to manufacturer's certificate.

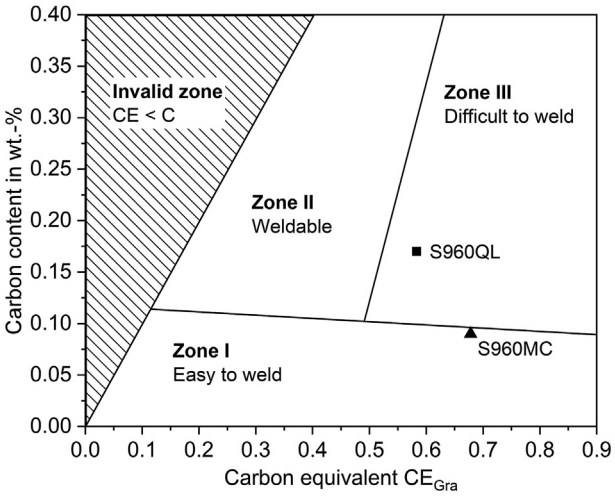

Fig. 2 – Classification of base materials according to Graville [26,51].

Table 1 – Chemical composition in wt.-% and calculated carbon equivalents of test materials measured by optical emission spectroscopy (Fe - balance).

Material	C	Si	Mn	Cr + Ni + Mo	V + Nb + Ti	CE_{Gra}[a]	CE_{IIW}[b]	CET[c]	P_{cm}[d]
S960MC	0.09	0.12	1.69	1.625	0.144	0.68	0.66	0.34	0.27
S960QL	0.17	0.22	1.23	0.857	0.054	0.58	0.55	0.36	0.30
FM	0.10	0.73	1.94	3.270	<0.100	0.90	0.78	0.43	0.32

[a] $CE_{Gra} = C + (Mn + Si)/6 + (Ni + Cu)/15 + (Cr + Mo + V)/5$ [26,51].
[b] $CE_{IIW} = C + Mn/6 + (Ni + Cu)/15 + (Cr + Mo + V)/5$ [52].
[c] $CET = C + (Mn + Mo)/10 + (Cr + Cu)/20 + Ni/40$ [52].
[d] $P_{cm} = C + (Mn + Cu + Cr)/20 + Si/30 + Ni/60 + Mo/15 + V/10 + 5B$ [51].

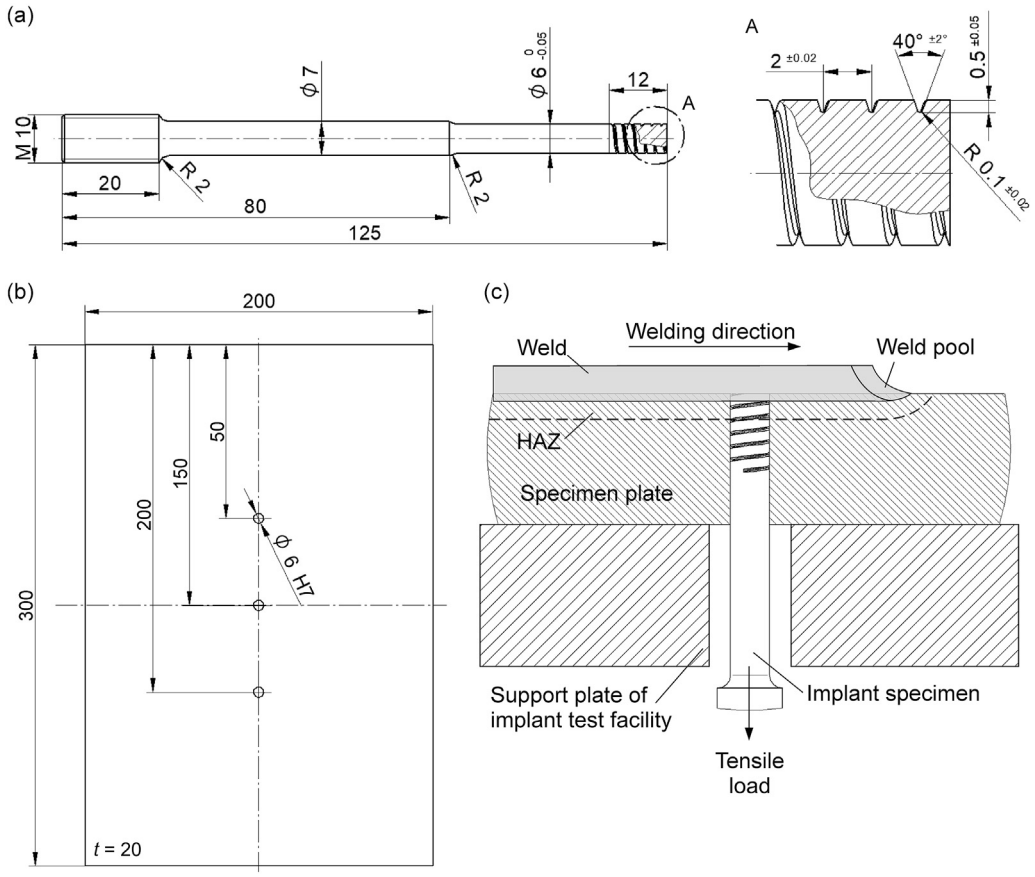

Fig. 3 – Schematic illustration of the implant test: (a) geometry of the implant specimen with detail of spiral notch, (b) geometry of support plate (c) test configuration; all dimensions in mm.

Table 3 – Welding parameters for the implant tests.

Wire feed speed v_D in m/min	Welding speed v_S in cm/min	Contact tube distance in mm	Arc voltage U in V	Welding current I in A	Energy input E in kJ/mm
8.7	27	17	26.2 ± 0.1	293 ± 10	1.7

Measurement of hydrogen in arc weld metal

To determine the hydrogen concentration in the arc weld metal, welds according to ISO 3690 [47] were carried out using the welding parameters from Table 3. For the examinations the ISO sample "B" was used with dimensions 15 mm × 30 mm × 10 mm of test specimen. The specimens were made of S690QL steel, which were degassed at a temperature of 650 °C for 1 h before welding. The oxide layer was then removed by grinding. For welding itself, specimens were clamped in a water-cooled welding fixture, see Fig. 4. Immediately after welding, the samples were removed from the welding fixture, quenched in ice water and stored in liquid nitrogen according to the standard. After the specimens were completely frozen, they were removed from liquid nitrogen and the starting and run off weld tabs were struck off with a hammer and the test specimens were frozen again. For hydrogen analyses, the frozen specimens were heated up for 60 s in ethanol to room temperature. Afterwards, the corresponding hydrogen amount in the specimen was determined

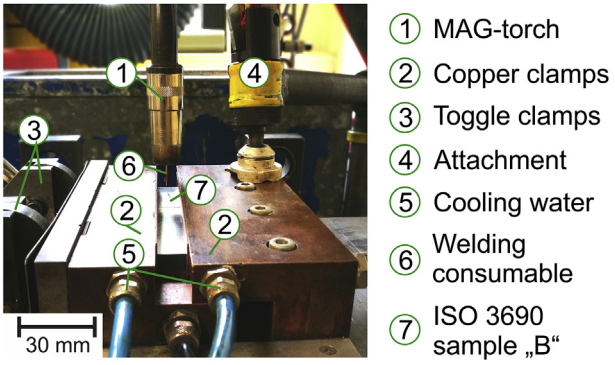

Fig. 4 – Welding fixture for ISO 3690 welding with clamped specimen [55].

by carrier gas hot extraction (CGHE) technique [55] using a G8 GALILEO analyzer from *Bruker AXS GmbH* (Karlsruhe, Germany). With this method, the specimens were heated up to 400 °C in an infrared furnace to collect the diffusible hydrogen.

To get information about the trapped hydrogen in the specimen, three other samples were analyzed at 900 °C for total hydrogen concentration. Contrary to the methods described in the standard [47], the effused hydrogen was detected using a quadrupole mass spectrometer (MS) ESD 1000 from *InProcess Instruments Gesellschaft für Prozessanalytik mbH* (Bremen, Germany). More details about MS principle can be found in Refs. [56,57]. The hydrogen concentration determined via MS is then calculated for each specimen according to Eq. (1):

$$H_D = I/(K \times m) \quad (1)$$

where I is the integrated ion current vs. time in A, K is the determined calibration factor in A/μg, and m is the weight of the arc weld metal in g. The weight used is the difference mass of the specimen before and after welding, which was determined by analytical balance XP205S from *Mettler-Toledo GmbH* (Giessen, Germany). The hydrogen concentration H_D is calculated in μg/g, which corresponds to 1 ppm or 1.11 ml/100 g of arc weld metal.

The use of MS is recommended for investigations for small specimen dimensions or to achieve small scattering of the measurement signals. Nevertheless, hydrogen detection by using CGHE and MS was already applied in some studies [15,17,56,57]. The results obtained with MS are comparable with those of other measurement methods [57].

Further investigations

As already mentioned, incipient cracks were used as an evaluation criterion. Therefore, two longitudinal sections of the unruptured specimens were machined via fine saw cut in each case 0.8 mm off-center. According to Ref. [53] metallographic examinations for incipient cracks at magnification factor of 400x and 600x were performed. In addition, metallographic examinations transverse to the welding direction were carried out to determine the fracture position of the fractured implant specimens. All metallographic specimens were embedded, ground, polished and etched with 2% Nital (HNO_3). Furthermore, hardness testing was carried out on one specimen each of TMCP and QT steel in the weld metal, HAZ and base material with a test load of 98.07 N (HV 10) and 9.807 N (HV 1). The analyses of fracture surfaces of fractured implant specimens were conducted by using the scanning electron microscope (SEM) Scios DualBeam from *Thermo Fisher Scientific* (Munich, Germany). An accelerated voltage of 20 kV was chosen for SEM imaging.

Results and discussion

Hydrogen concentration in arc weld metal

In the implant test, diffusible hydrogen in arc weld metal diffuses during cooling into the notch area of the implant specimen located in the HAZ. When investigating HAC susceptibility it is therefore important to indicate the hydrogen concentration in the respective tests. Table 4 gives an overview about the measured hydrogen concentrations in the arc weld metal. Total hydrogen concentration H_{tot} of 2.00 ml/100 g was determined. This amount of hydrogen is already captured in the solid wire when the filler material is delivered [15]. About 17% of the introduced hydrogen is trapped in the weld metal, so the diffusible hydrogen concentration H_D is 1.66 ml/100 g. As the weld metal contains fine precipitates of type AlN, TiN and V (C, N) for realizing high strengths and good toughness [5,6], hydrogen is deeply trapped and becomes mobile again only with high energy input [58,59]. The trapping results in a reduction of the diffusible hydrogen concentration. However, due to the complexity of the microstructure in the weld metal, hydrogen diffusion is slowed down significantly, which increases the risk of delayed HAC. Nevertheless, the tested QT steel shows remarkable degradation of the mechanical properties in the HAZ at the determined diffusible hydrogen level [10,11].

Implant test results

Fig. 5 shows the results of the implant tests as a plot of applied implant stress vs. TTF for both tested materials. The respective cooling times are also indicated. In both test series there are approximately equal $t_{8/5}$-cooling times of 7 s. This is within the working range of the materials used and the microstructure in the weld metal consists mainly of martensite and bainite [18]. The microstructure of the HAZ will be discussed later. Furthermore, a stable arc process can be assumed in both test series due to the low scattering of the $t_{3/1}$-cooling times, which is why the scattering of the measuring points in the diagrams is also relatively low. For the S960QL in Fig. 5(a), a significant increase in TTF with reduction of the applied implant stress can be seen. The diffusion-controlled process of HAC can therefore be clearly observed. At the highest applied implant stress of 905 MPa the TTF is only 59 min. With decreased implant stress of 605 MPa, which is the LCS, TTF increases to 676 min. The specimens loaded below LCS

Table 4 – Diffusible and total hydrogen concentration in arc weld metal.

Analyzing temperature in °C	Hydrogen concentration in ml/100 g			Mean hydrogen concentration in ml/100 g	Standard deviation
	Trial 1	Trial 2	Trial 3		
400 (H_D)	1.71	1.64	1.63	1.66	0.04
900 (H_{tot})	2.19	1.87	1.93	2.00	0.14

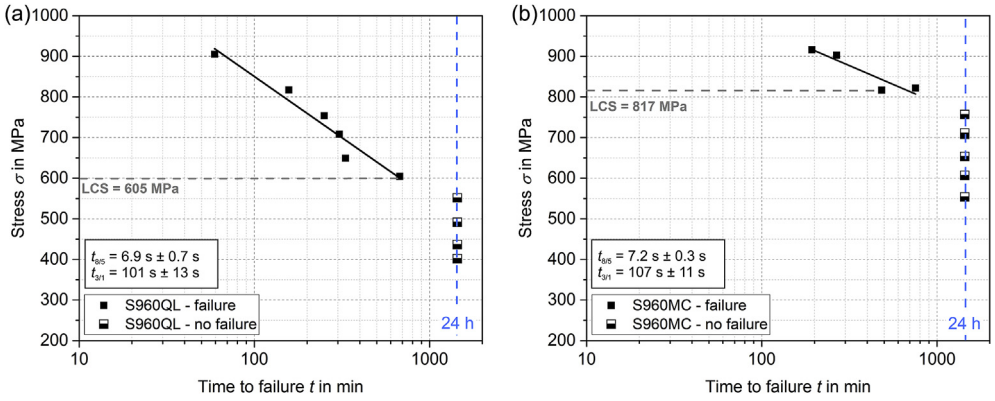

Fig. 5 – Implant test results of applied stress vs. time to failure for the two test materials: (a) S960QL, (b) S960MC; half-filled symbols indicate that specimen did not fail within 24 h.

showed no fracture after 24 h. Van den Eeckhout et al. [60] observed an increased hydrogen diffusivity with increased applied elastic stress on tensile samples. The elastic tensile stress expands the crystallographic lattice which increases the hydrogen diffusion. This in turn means in the case of the implant test that the TTF increases with decreasing applied stress. The results of the test series with S960MC also show an increase in TTF with reduced applied implant stress, see Fig. 5(b). However, the LCS of 817 MPa is significantly higher compared to LCS of S960QL. Implant stresses below LCS did not result in fracture within 24 h. At the highest stress of 903 MPa, the TTF is already 267 min, which is four to five times the TTF at LCS of the S960QL. This fact was also reported in Ref. [44] with smaller time difference due to significantly increased hydrogen concentration of 6.5 ml/100 g in arc weld metal. Also, the LCS are increased compared to the LCS in Fig. 5, as steels with lower strength were investigated. Because of the significant shift of TTF to longer times and the significantly higher LCS, it can be concluded that the S960MC has a better resistance to HAC in the HAZ than the S960QL. This is also illustrated by the ratio of LCS to nominal yield strength (960 MPa), which is referred to in literature as normalized critical stress ratio (NCSR). The NCSR is 0.63 and 0.85 for the S960QL and for the S960MC, respectively. The results are in good agreement with investigations by Yue et al. [44,45] analyzing the HAC susceptibility in the HAZ by implant tests of 690 MPa grade QT and TMCP steel.

Fig. 6 shows cross sections transverse to welding direction to determine the fracture position of the implant specimens. The geometry of the implant specimen before loading was applied is indicated in both parts. Fracturing occurred in the HAZ at the notch root of the implant specimen through the weld metal for S960QL as well as for S960MC. This behavior was observed for all welded specimens. The reasons are explained in the following.

Weld microstructure and incipient cracks

Since the distinction between martensite and bainite in ferritic materials is very difficult by light optical microscopy, the microstructure in the CGHAZ was analyzed by means of hardness testing and calculated maximum hardness for a purely martensitic and bainitic microstructure according to Dueren [61]. Based on this, the maximum hardness values in the HAZ can be calculated as a function of the chemical composition using Eqs. (2) and (3):

$$HV_M = 802 \text{ x } C + 305 \quad (2)$$

$$HV_B = 350 \text{ x } (C + Si/11 + Mn/8 + Cu/9 + Cr/5 + Ni/17 + Mo/6 + V/3) + 101 \quad (3)$$

where HV_M is the hardness for 100% martensite and HV_B is the hardness for 100% bainite. The elements are inserted in wt.-%. Hardness values of 441 HV 10 (HV_M) and 276 HV 10 (HV_B) result for the S960QL. For the S960MC, HV_M is 377 HV 10 and HV_B is 312 HV 10. In Yurioka's calculation formulas [62], the elements Nb and B are also considered for the maximum hardness. However, this results in the same values.

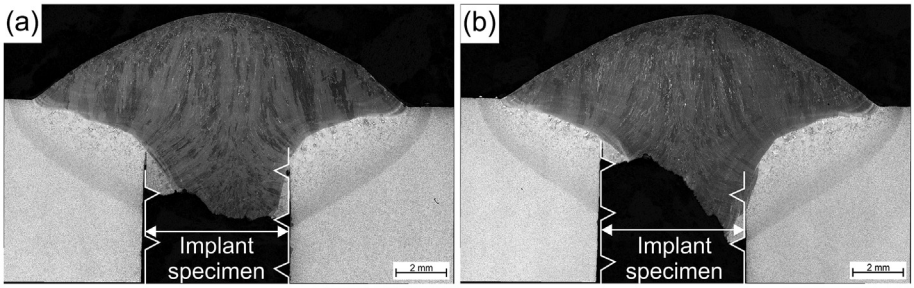

Fig. 6 – Cross section to determine the fracture position of the implant specimens: (a) S960QL, (b) S960MC.

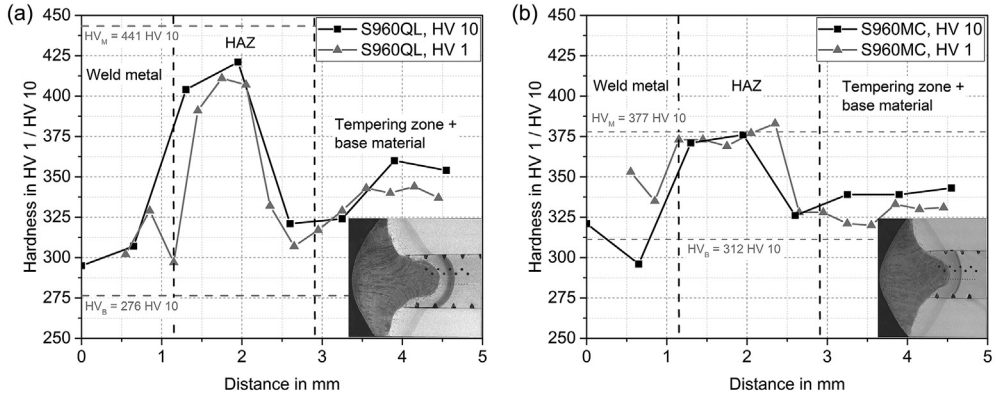

Fig. 7 – Vickers hardness measurement along the axis of implant specimen with indication of the hardness for a purely bainitic (HV_B) or purely martensitic (HV_M) microstructure in the HAZ according to Ref. [61]: (a) S960QL, (b) S960MC; micrographs in the bottom right-hand corner of the diagrams show the position of the hardness indentations.

Fig. 7 shows Vickers hardness distributions in HV 1 and HV 10 across the weld metal, HAZ and base material as well as the calculated hardness values HV_M and HV_B for the HAZ for both tested materials. In case of S960QL, the hardness in base material is 357 HV 10, which increases in the CGHAZ to a maximum of 421 HV 10 and the mean value is 301 HV 10 in weld metal, see Fig. 7(a). It is also shown that from the CGHAZ the hardness decreases to the fine-grained HAZ (FGHAZ) into the inter-critical HAZ (ICHAZ) to a minimum of 321 HV 10. This minimum is lower than the hardness of the base material. The HV 1 hardness distribution shows this softening even more clearly. As the maximum hardness of 421 HV 10 in CGHAZ is lower than HV_M, which is 441 HV 10, a mixed microstructure containing primarily martensite and small amounts of bainite is present. The hardness distribution of S960MC specimen shows a different behavior, see Fig. 7(b). The hardness in the base material is 340 HV 10, increases to a maximum of 376 HV 10 in the HAZ and is lowered to 309 HV 10 in the weld metal. Because the same welding parameters and the same filler material were used as in the tests with the S960QL, the respective hardness values in the weld metal are approximately the same. The hardness of the base material of S960MC is slightly lower than the hardness in base material of S960QL. However, the hardness values in the HAZ differ significantly from S960MC and S960QL. Due to the comparatively low carbon content of S960MC, there is no such drastic hardening in the HAZ. In addition, the hardness level of CGHAZ is at same level as the FGHAZ. Softening, like in the S960QL, hardly exists due to higher V and Cr content of S960MC [63]. These carbide-forming alloying elements lead to better resistance to tempering softening. The maximum hardness in CGHAZ of 376 HV 10 corresponds to HV_M, but in the HV 1 hardness distribution a slight increase in hardness from fusion line towards the base material can be observed. The calculation according to Ref. [61] only provides an estimation. Hence, the microstructure of CGHAZ of S960MC also consists of a mixed structure of primarily martensite, small amounts of bainite and auto tempered martensite.

Table 5 gives a summary of the hardness measurements. It also includes the amount of hardening (hardness difference between base material and CGHAZ) and the amount of softening (hardness difference between base material and minimum hardness). It is clearly shown here that S960QL has a significant hardening in the CGHAZ of 64 HV 10 and a considerable softening in ICHAZ of 36 HV 10.

The CGHAZ is the critical location regarding HAC. This is where the highest hardness occurs with a mainly martensitic phase and crack initiation at notched area takes place, cf. Fig. 6. Therefore, the microstructure and its consequences for HAC behavior will be discussed in the following. Fig. 8 illustrates light optical microscopic (LOM) images of the CGHAZ of both test materials. As already mentioned, in both cases a bainitic phase exists in addition to the martensitic phase. Looking purely visually at the images, it is noticeable that the CGHAZ of the S960QL (Fig. 8(a)) has a significantly larger grain size compared to the S960MC (Fig. 8(b)). This fact has already been demonstrated on similar materials of lower strength in Refs. [25,29].

The higher Ti content of S960MC compared to S960QL can lead to precipitation of Ti-rich carbonitrides [22,29]. Their extremely high temperature stability results in a fine-grained CGHAZ. During weld thermal cycle, pinning effects slow down the growth of the austenite grains. The particles can even be seen in the images by LOM as also reported in Refs. [29,64], see Fig. 8(b). The grain size can have a significant influence on trapping behavior of hydrogen and thus also on HAC [30,31]. The amount of diffusible hydrogen per unit grain boundary area is lower with decreased grain size. In addition, S960MC

Table 5 – Hardness in HV 10 across the weld.

Test series	Hardness in weld metal	Maximum hardness in CGHAZ	Minimum hardness in HAZ	Hardness of base material	Amount of hardening	Amount of softening
S960QL	301 ± 8	421	321	357 ± 4	64 (18%)	36 (10%)
S960MC	309 ± 18	376	326	340 ± 2	36 (11%)	14 (4%)

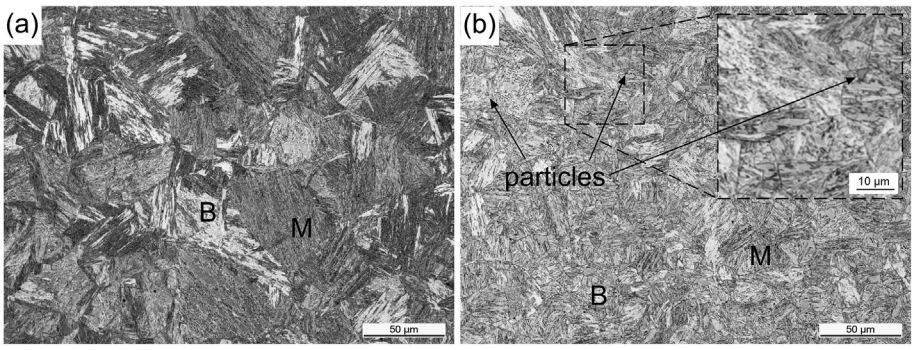

Fig. 8 – Microstructure in the CGHAZ: (a) S960QL, (b) S960MC; B and M are bainite and martensite; Particles are Ti-rich carbides or nitrides.

also contains a higher V content which in combination with Ti also leads to strong trapping [58,59]. In particular, the Ti-rich precipitates cause deeply irreversible trapping [65]. These facts lead to a higher plastic deformation and thus, grain refinement with existing precipitates can lead to better HAC resistance in the HAZ of S960MC compared to S960QL.

The area of the notch of the implant specimen represents a triaxially stressed region. Introduced hydrogen diffuses from weld metal during cooling into this highly stressed area. Thus, there is a critical combination of the three influencing factors on HAC in the CGHAZ at the notch root: a mainly martensitic microstructure with high hardness, a mechanically strained area and a locally increased hydrogen concentration. As a result, micro-cracks (incipient cracks) arise at this point, which propagate into the weld metal. Fig. 9 shows an incipient crack in welded implant sample after 24 h of loading in welding direction as an example. In case of S960QL, the maximum applied implant stress σ_{crit} at which no more cracking occurred is 402 MPa. For the S960MC, σ_{crit} is increased to 554 MPa. This is, besides NCSR, another factor showing the better HAC resistance in the HAZ of S960MC.

Fractography

The topography of the fracture surfaces of the ruptured implant specimens was carried out by SEM. Fig. 10(a)-(d) show the fracture topography of implant specimen of S960QL. The fracture surface is separated into different areas with different topography, see Fig. 10(a). The area of crack initiation was also localized. The fracture surface of incipient crack shows a quasi-cleavage (QC) topography with secondary cracks, see Fig. 10(b) and (c). The topography in the transition zone was ductile with micro-void coalescence (MVC) and QC. The remaining fracture topography was ductile with MVC, see Fig. 10(d). The fracture topography of implant specimen of S960MC is shown in Fig. 11(a)-(d). In this case only two different areas could be identified, which are marked in Fig. 11(a). The topography of incipient crack was QC with secondary cracks, see Fig. 11(b). Compared to S960QL, a higher level of deformation was observed in this area, cf. Fig. 11(c). The remaining fracture topography was also ductile with MVC, see Fig. 11(d). A transition zone from QC to MVC could not be located for S960MC.

HAC with QC topography on the fracture surface is common for low carbon steels [66]. The different fracture

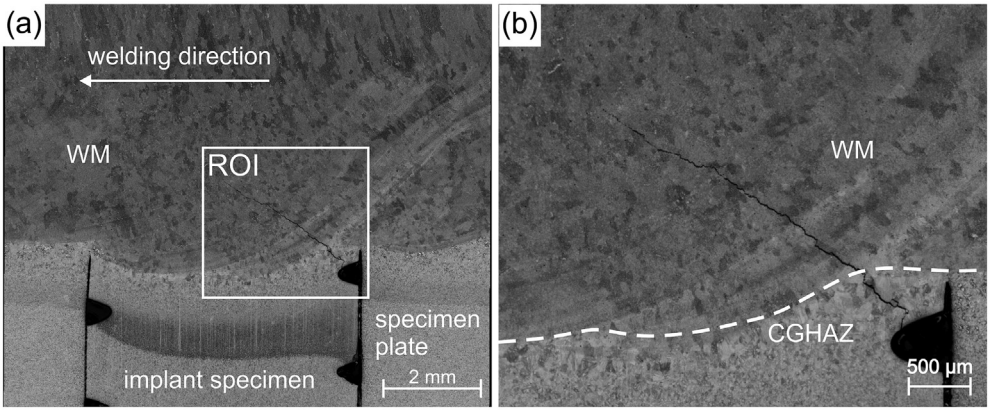

Fig. 9 – Incipient crack in implant sample in weld metal (WM) and CGHAZ after 24 h of loading: (a) LOM image with region of interest (ROI), (b) ROI in detail with incipient crack; $\sigma = 492$ MPa (S960QL).

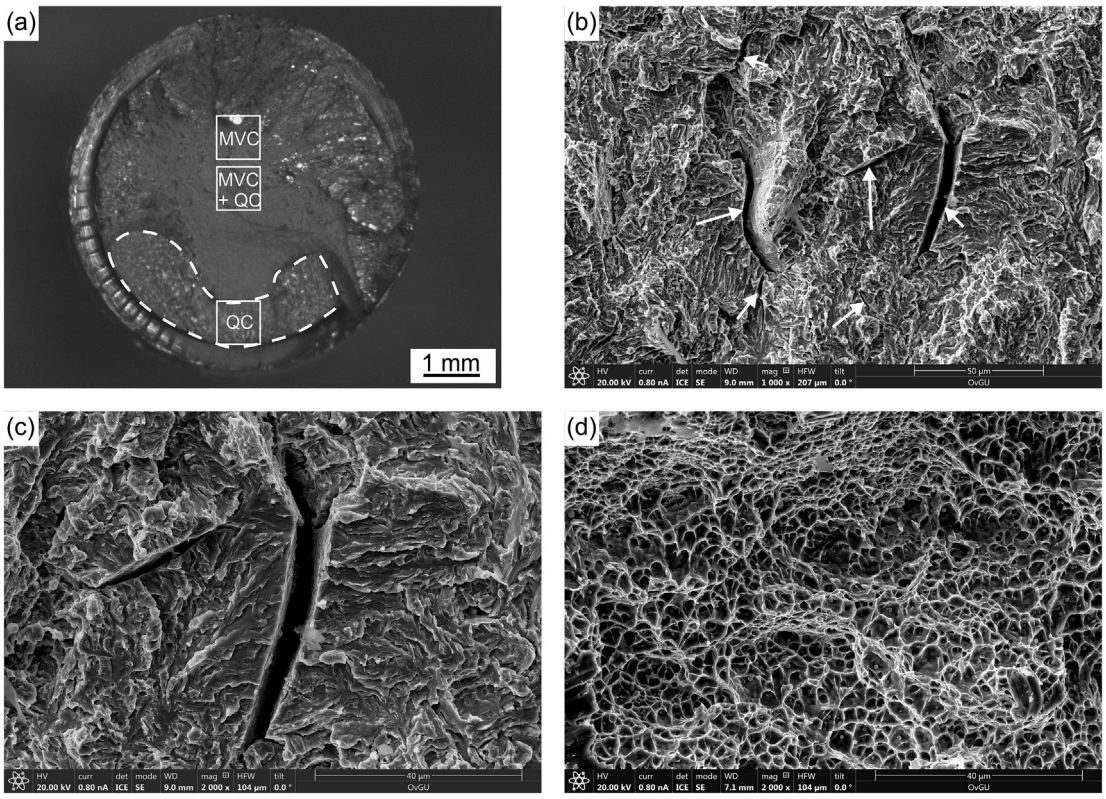

Fig. 10 – Fracture topography of implant specimen of S960QL (σ = 708 MPa): (a) light optical fracture overview with three regions of interest (dotted area highlights the area of crack initiation), (b) QC: quasi-cleavage, (c) QC at higher magnification, (d) MVC: micro-void coalescence; white arrows in (b) indicate secondary cracks.

appearance of QC and MVC can be explained by Beachem's model [67], which was substantiated by Gedeon and Eagar on implant tests [68]. The fracture topography depends on the interaction of diffusible hydrogen and stress intensity. After the implant specimen is loaded, hydrogen concentration at the notch root is not high enough to initiate cracking. During an incubation period, mobile hydrogen diffuses from the weld metal into this triaxially stressed region until a critical concentration for crack initiation is reached in the CGHAZ. The crack appears as QC topography first. As crack propagation continues, the stress intensity factor is increasing, and the hydrogen concentration is decreasing at the crack tip. This leads to MVC fracture mode until complete fracture of the implant sample takes place.

The origin of the QC fracture surface has been interpreted by Martin et al. [69,70]. Hence, voids and micro-cracks are formed along the intersection of slip bands. The role of hydrogen is to support the development of the intense slip bands and to reduce the stress required to create the initial voids and cracks. This process is characterized by plastic deformations, which are enhanced and accelerated by hydrogen. Moreover, Guedes et al. [71] showed in tempered martensitic steel that trapped hydrogen result in ductile damage with MVC and mobile hydrogen in QC fracture. Both theories can explain the higher deformation on the QC fracture of S960MC compared to S960QL. The higher density of precipitates and the higher grain boundary area of S960MC can lead to increased hydrogen trapping, so that the mobile hydrogen content is reduced. This leads to an increased amount of MVC and QC fracture with more deformation.

Rating of HAC susceptibility in the HAZ

In the following, the results from the implant investigations are presented as a comparison between the materials S960QL and S960MC. Fig. 12 shows the applied implant stress vs. TTF. It can be clearly seen that the S960MC has longer TTF of about 130 min–330 min compared to S960QL. In addition, the samples welded with S960MC show a significantly higher LCS as well as a higher critical implant stress σ_{crit}. This leads to the conclusion, that the S960MC has a better resistance to HAC in the HAZ than the S960QL at the given diffusible hydrogen concentration H_D of 1.66 ml/100 g in arc weld metal.

The most important results are summarized in Table 6. Using ISO 18265 [72] the maximum hardness in CGHAZ was converted to the tensile strength of CGHAZ. In the case of S960QL the tensile strength is 1353 MPa, for the S960MC it is 1208 MPa. The ratio of the critical implant stress σ_{crit} to the tensile strength of CGHAZ gives the embrittlement index (EI). The EI is 0.30 and 0.46 for the S960QL and for the S960MC, respectively. The higher EI indicates a better resistance to HAC. In addition to NCSR, this is a further evaluation criterion to show that the S960QL is more susceptible to HAC in the HAZ. It must be mentioned that this behavior is at first only valid for the above-mentioned diffusible hydrogen concentration and for the used welding parameters and cooling

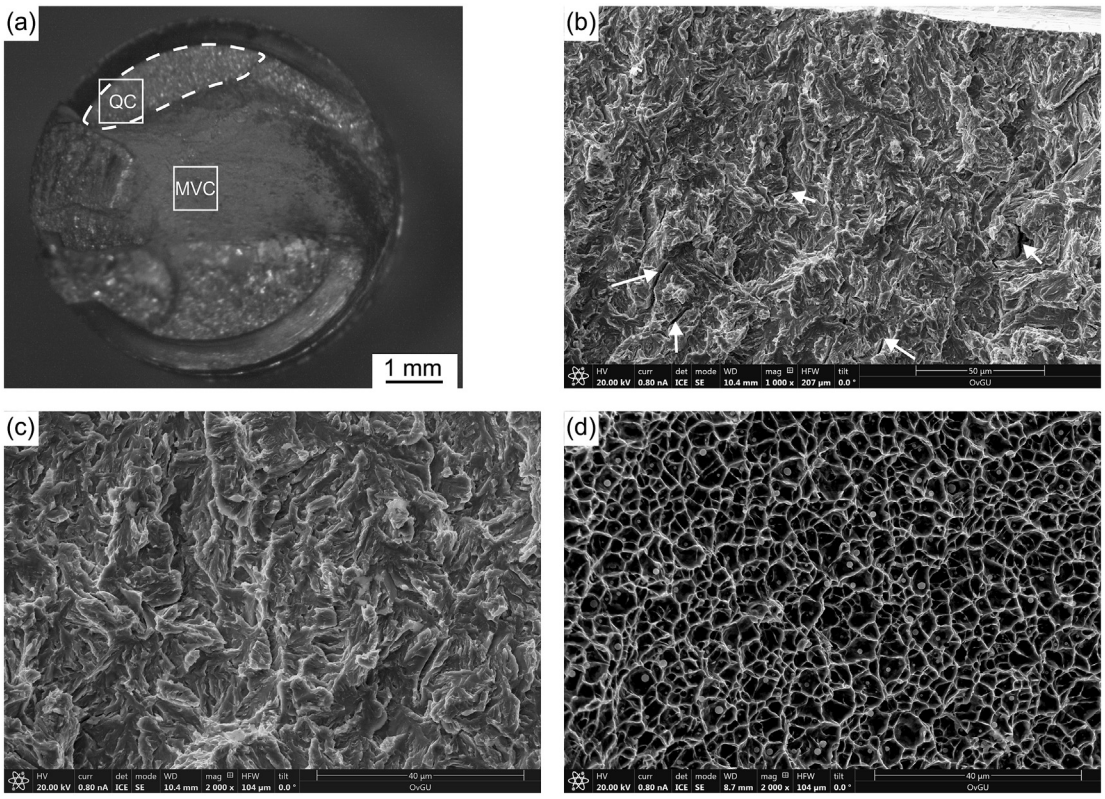

Fig. 11 – Fracture topography of implant specimen of S960MC (σ = 903 MPa): (a) light optical fracture overview with two regions of interest (dotted area highlights the area of crack initiation), (b) QC: quasi-cleavage, (c) QC at higher magnification, (d) MVC: micro-void coalescence; white arrows in (b) indicate secondary cracks.

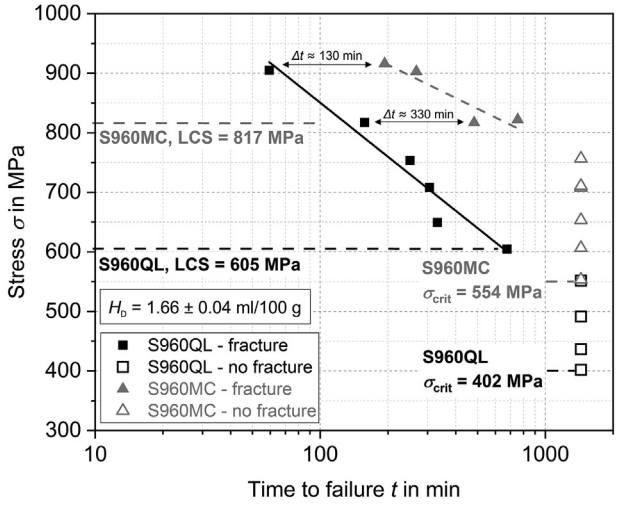

Fig. 12 – Comparison of implant test results of applied stress vs. time to failure with critical implant stress σ_{crit}.

times. In order to be able to make far-reaching statements, it would be necessary also to consider the influence of preheating temperatures, heat input and different filler materials as well as different sheet thicknesses of base materials.

As already mentioned in the introduction, previous research using the implant test dealt with the susceptibility to HAC in the HAZ of QT and TMCP steels with a yield strength ≤ 690 MPa [44–46]. With the present study, the area of research is expanded by 960 MPa grade steels. Fig. 13 shows the results from Refs. [44,46] together with the present study regarding NCSR and EI. The hydrogen concentrations present in the investigations are different in each case, but, are within a critical range for degradation of the respective material. With increasing strength of the base materials, degradation of the HAZ increases in terms of decreasing NCSR or EI. In other words, the critical stress for complete fracture in relation to nominal yield strength or the critical stress for crack initiation in relation to the strength of the CGHAZ decreases with increasing strength of base material. NCSR > 1 is due to the fact, that the nominal yield strength instead of the real yield strength is used for calculation of NCSR, as is the case with 690 MPa grade TMCP steel. Steels with a nominal yield strength of 960 MPa show the highest degradation of HAZ in implant tests. However, in the tests TMCP steels show a reduced risk to HAC compared to QT steels for the used parameters. Finally, it can be said that the Graville diagram in Fig. 2 can be applied to modern high-strength steels with nominal yield strength of 960 MPa, which Yue et al. [44,45]

Table 6 – Implant test results.

Material	CGHAZ max hardness in HV 10	CGHAZ tensile strength[a] in MPa	Lower critical stress (LCS)in MPa	Critical implant stress σ_{crit} in MPa	Normalized critical stress ratio (NCSR)[b]	Embrittlement index (EI)[c]
S960QL	421	1353	605	402	0.63	0.30
S960MC	376	1208	817	554	0.85	0.46

[a] Conversion from max hardness in CGHAZ according to ISO 18265.
[b] LCS normalized to the nominal yield strength of the base material (960 MPa).
[c] Critical implant stress normalized to calculated CGHAZ tensile strength.

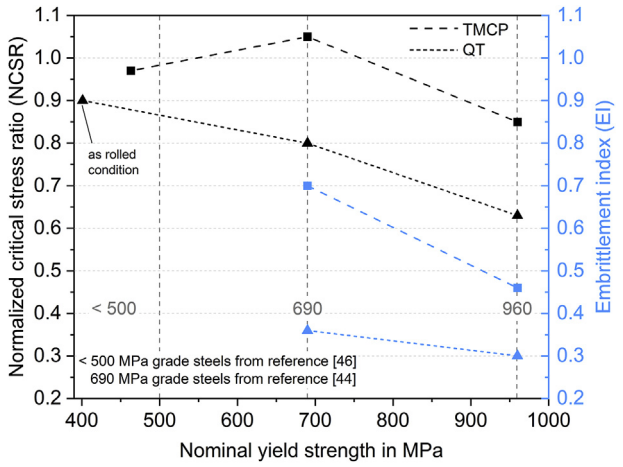

Fig. 13 – Normalized critical stress ratio and embrittlement index for HAZ of different steel grades.

already demonstrated on steels with nominal yield strength of 690 MPa.

Conclusions

The results of this work contribute to the estimation of the HAC susceptibility in the HAZ of high-strength steels with a nominal yield strength of 960 MPa. In these investigations, the focus of research was on the influence of the microstructure (chemical composition) on HAC behavior. For this purpose, a comparison of the quenched and tempered steel S960QL and the thermo-mechanical controlled processed steel S960MC was carried out by using the externally loaded implant test. Under the welding conditions used, the following conclusions can be drawn from the study:

- The maximum hardness in the CGHAZ is 421 HV 10 and 376 HV 10 for S960QL and S960MC, respectively.
- The CGHAZ of both materials consists mainly of martensite. The grain size in the CGHAZ of S960MC is smaller than that of S960QL.
- Cracking in all implant specimens occurred in the notch root in the CGHAZ. Crack propagation took place from the initial crack into the weld metal.
- Lower critical stress (LCS) for complete fracture was determined to be 605 MPa and 817 MPa for S960QL and S960MC, respectively. Critical implant stress σ_{crit} at which nor more cracking occurred is 402 MPa and 554 MPa for S960QL and S960MC, respectively.
- Normalized critical stress ratio (NCSR) was determined to be 0.63 for the S960QL and 0.85 for the S960MC. The embrittlement index (EI) was calculated and resulted in 0.30 for the S960QL and 0.46 for the S960MC. Both, the higher NCSR and the higher EI indicate a better resistance to HAC in the HAZ of the S960MC.
- Implant specimens of S960MC showed a significantly increased time to failure compared to S960QL. The fracture surfaces showed QC and MVC fracture for both materials. QC fracture was found with secondary cracks on the surface of incipient cracks. However, the fracture surfaces of S960QL showed higher degradation with reduced deformation than the fracture surfaces of S960MC.

Funding

This research did not receive any specific grant from funding agencies in the public, commercial, or not-for-profit sectors.

Acknowledgements

The authors would like to thank Hamza Yahyaoui from BAM for his assistance with the implant tests. Dirk Miessner and Markus Wilke from Otto von Guericke University are thanked for the metallographic analyses and for the SEM investigations.

REFERENCES

[1] Ahlblom B, Hansson P, Narström T. Martensitic structural steels for increased strength and wear resistance. Mater Sci Forum 2007;539–543:4515–20. https://doi.org/10.4028/www.scientific.net/MSF.539-543.4515.
[2] Hulka K, Kern A, Schriever U. Application of niobium in quenched and tempered high-strength steels. Mater Sci Forum 2005;500–501:519–26. https://doi.org/10.4028/www.scientific.net/MSF.500-501.519.
[3] Węglowski MS, Zeman M. Prevention of cold cracking in ultra-high strength steel Weldox 1300. Arch Civ Mech Eng 2014;14:417–24. https://doi.org/10.1016/j.acme.2013.10.010.
[4] Schneider C, Ernst W, Schnitzer R, Staufer H, Vallant R, Enzinger N. Welding of S960MC with undermatching filler material. Weld World 2018;62:801–9. https://doi.org/10.1007/s40194-018-0570-1.

[5] Holly S, Haslberger P, Zügner D, Schnitzer R, Kozeschnik E. Development of high-strength welding consumables using calculations and microstructural characterisation. Weld World 2018;62:451–8. https://doi.org/10.1007/s40194-018-0562-1.

[6] Schnitzer R, Zügner D, Haslberger P, Ernst W, Kozeschnik E. Influence of alloying elements on the mechanical properties of high-strength weld metal. Sci Technol Weld Join 2017;22:536–43. https://doi.org/10.1080/13621718.2016.1274095.

[7] Yurioka N, Suzuki H. Hydrogen assisted cracking in C-Mn and low alloy steel weldments. Int Mater Rev 1990;35:217–49. https://doi.org/10.1179/imr.1990.35.1.217.

[8] Lynch S. Hydrogen embrittlement phenomena and mechanisms. Corrosion Rev 2012;30:105–23. https://doi.org/10.1515/corrrev-2012-0502.

[9] Djukic MB, Bakic GM, Zeracic VS, Sedmak A, Rajicic B. The synergistic action and interplay of hydrogen embrittlement mechanisms in steels and iron: localized plasticity and decohesion. Eng Fract Mech 2019;216:106528. https://doi.org/10.1016/j.engfracmech.2019.106528.

[10] Rhode M, Steger J, Boellinghaus T, Kannengiesser T. Hydrogen degradation effects on mechanical properties in T24 weld microstructures. Weld World 2016;60:201–16. https://doi.org/10.1007/s40194-015-0285-5.

[11] Zimmer P, Seeger DM, Boellinghaus T. Hydrogen permeation and related material properties of high strength structural steels. In: Cerjak HH, Enzinger N, editors. High strength steels for hydropower plants. Graz: Verlag der Techn. Univ. Graz; 2005. p. 1–18. paper 17.

[12] Villalobos JC, Del-Pozo A, Mayen J, Serna S, Campillo B. Hydrogen embrittlement susceptibility on X-120 microalloyed steel as function of tempering temperature. Int J Hydrogen Energy 2020;45:9137–48. https://doi.org/10.1016/j.ijhydene.2020.01.094.

[13] Pandey C, Mahapatra MM, Kumar P, Saini N. Effect of weld consumable conditioning on the diffusible hydrogen and subsequent residual stress and flexural strength of multipass welded P91 steels. Metall Mater Trans B 2018;49B:2881–95. https://doi.org/10.1007/s11663-018-1314-8.

[14] Kannengiesser T, Lausch T. Diffusible hydrogen content depending on welding and cooling parameters. Weld World 2012;56:26–33. https://doi.org/10.1007/BF03321392.

[15] Schaupp T, Rhode M, Kannengiesser T. Influence of welding parameters on diffusible hydrogen content in high-strength steel welds using modified spray arc process. Weld World 2018;62:9–18. https://doi.org/10.1007/s40194-017-0535-9.

[16] Świerczyńska A, Fydrych D, Rogalski G. Diffusible hydrogen management in underwater wet self-shielded flux cored arc welding. Int J Hydrogen Energy 2017;42:24532–40. https://doi.org/10.1016/j.ijhydene.2017.07.225.

[17] Schaupp T, Rhode M, Yahyaoui H, Kannengiesser T. Influence of heat control on hydrogen distribution in high-strength multi-layer welds with narrow groove. Weld World 2019;63:607–16. https://doi.org/10.1007/s40194-018-00682-0.

[18] Schroepfer D, Kromm A, Schaupp T, Kannengiesser T. Welding stress control in high-strength steel components using adapted heat control concepts. Weld World 2019;63:647–61. https://doi.org/10.1007/s40194-018-00691-z.

[19] Pandey C, Mahapatra MM, Kumar P, Saini N, Srivastava A. Microstructure and mechanical property relationship for different heat treatment and hydrogen level in multi-pass welded P91 steel joint. J Manuf Process 2017;28:220–34. https://doi.org/10.1016/j.jmapro.2017.06.009.

[20] Klein M, Rauch R, Spindler H, Stiaszny P. Ultra high strength steels produced by thermomechanical hot rolling – advanced properties and applications. BHM Berg- Hüttenmännische Monatsh 2012;157:108–12. https://doi.org/10.1007/s00501-012-0062-3.

[21] Villalobos JC, Del-Pozo A, Campillo B, Mayen J, Serna S. Microalloyed steels through history until 2018: review of chemical composition, processing and hydrogen service. Metals 2018;8:351. https://doi.org/10.3390/met8050351.

[22] Zhang L, Kannengiesser T. Austenite grain growth and microstructure control in simulated heat affected zones of microalloyed HSLA steel. Mater Sci Eng A 2014;613:326–35. https://doi.org/10.1016/j.msea.2014.06.106.

[23] Easterling K. Introduction to the physical metallurgy of welding. 2nd ed. Oxford: Butterworth-Heinemann Ltd; 1992.

[24] Schaupp T, Schroepfer D, Kromm A, Kannengiesser T. Welding residual stresses in 960 MPa grade QT and TMCP high-strength steels. J Manuf Process 2017;27:226–32. https://doi.org/10.1016/j.jmapro.2017.05.006.

[25] Yue X, Lippold JC, Alexandrov BT, Babu SS. Continuous cooling transformation behavior in the CGHAZ of naval steels. Weld J 2012;91:67s–75s.

[26] Graville BA. Cold cracking in welds in HSLA steels - proceedings of an international conference, 9-12 november 1976, rome, Italy. In: Rothwell AB, Malcolm Gray J, editors. Welding of HSLA (microalloyed) structural steels. Ohio: American Society for Metals; 1978. p. 85–101.

[27] Grabke HJ, Riecke E. Absorption and diffusion of hydrogen in steels. Mater Tehnol 2000;34:331–42.

[28] Padhy GK, Ramasubbu V, Parvathavarthini N, Wu CS, Albert SK. Influence of temperature and alloying on the apparent diffusivity of hydrogen in high strength steel. Int J Hydrogen Energy 2015;40:6714–25. https://doi.org/10.1016/j.ijhydene.2015.03.153.

[29] Steppan E, Mantzke P, Steffens BR, Rhode M, Kannengiesser T. Thermal desorption analysis for hydrogen trapping in microalloyed high-strength steels. Weld World 2017;61:637–48. https://doi.org/10.1007/s40194-017-0451-z.

[30] Park C, Kang N, Liu S. Effect of grain size on the resistance to hydrogen embrittlement of API 2W Grade 60 steels using in situ slow-strain-rate testing. Corrosion Sci 2017;128:33–41. https://doi.org/10.1016/j.corsci.2017.08.032.

[31] Zan N, Ding H, Guo X, Tang Z, Bleck W. Effects of grain size on hydrogen embrittlement in a Fe-22Mn-0.6C TWIP steel. Int J Hydrogen Energy 2015;40:10687–96. https://doi.org/10.1016/j.ijhydene.2015.06.112.

[32] Thomas A, Szpunar JA. Hydrogen diffusion and trapping in X70 pipeline steel. Int J Hydrogen Energy 2020;45:2390–404. https://doi.org/10.1016/j.ijhydene.2019.11.096.

[33] Kannengiesser T, Boellinghaus T. Cold cracking tests—an overview of present technologies and applications. Weld World 2013;57:3–37. https://doi.org/10.1007/s40194-012-0001-7.

[34] Kurji R, Coniglio N. Towards the establishment of weldability test standards for hydrogen-assisted cold cracking. Int J Adv Manuf Technol 2015;77:1581–97. https://doi.org/10.1007/s00170-014-6555-3.

[35] Granjon HG. The 'implants' method for studying the weldability of high strength steels. Met Constr-Brit Weld 1969;1:509–15.

[36] Dickinson DW, Ries GD. Implant testing of medium to high strength steel-A model for predicting delayed cracking susceptibility. Weld J 1979;59:205s–11s.

[37] Sawhill Jr JM, Dix AW, Savage WF. Modified implant test for studying delayed cracking. Weld J 1974;53:554s–60s.

[38] Pandey C, Saini N, Mahapatra MM, Kumar P. Hydrogen induced cold cracking of creep resistant ferritic P91 steel for different diffusible hydrogen levels in deposited metal. Int J Hydrogen Energy 2016;41:17695–712. https://doi.org/10.1016/j.ijhydene.2016.07.202.

[39] Saini N, Pandey C, Mahapatra MM. Effect of diffusible hydrogen content on embrittlement of P92 steel, I0,46nt. J Hydrogen Energ 2017;42:17328–38. https://doi.org/10.1016/j.ijhydene.2017.05.214.
[40] Saini N, Mulik RS, Mahapatra MM. Effect of welding process parameters on embrittlement of Grade P92 steel using Granjon implant testing of welded joints. Int J Hydrogen Energy 2020;45:10189–98. https://doi.org/10.1016/j.ijhydene.2020.01.146.
[41] Savage WF, Nippes EF, Sawhill Jr JM. Hydrogen induced cracking during implant testing of alloy steels. Weld J 1976;55:400–7.
[42] Reddy GM, Mohandas T, Sarma DS. Cold cracking studies on low alloy steel weldments: effect of filler metal composition. Sci Technol Weld Join 2003;8:407–14. https://doi.org/10.1179/136217103225005552.
[43] Yadav U, Pandey C, Saini N, Thakre JG, Mahapatra MM. Study on hydrogen-assisted cracking in high-strength steels by using the Granjon implant test. Metallogr Microstruct Anal 2017;6:247–57. https://doi.org/10.1007/s13632-017-0351-z.
[44] Yue X. Investigation on heat-affected zone hydrogen-induced cracking of high-strength naval steels using the Granjon implant test. Weld World 2015;59:77–89. https://doi.org/10.1007/s40194-014-0181-4.
[45] Yue X, Feng XL, Lippold JC. Quantifying heat-affected zone hydrogen-induced cracking in high-strength naval steels. Weld J 2013;92:265s–73s.
[46] Kang Y, Kim M, Kim G, Kim N, Song S. Characteristics of susceptible microstructure for hydrogen-induced cracking in the coarse-grained heat-affected zone of carbon steel. Metall Mater Trans 2020;51:2143–53. https://doi.org/10.1007/s11661-020-05671-x.
[47] ISO 3690, Welding and allied processes - determination of hydrogen content in arc weld metal. 2018.
[48] EN 10025-6. Hot rolled products of structural steels - Part 6: technical delivery conditions for flat products of high yield strength structural steels in the quenched and tempered condition. 2020.
[49] EN 10149-2. Hot rolled flat products made of high strength steels for cold forming - Part 2: technical delivery conditions for thermomechanically rolled steels. 2013.
[50] ISO 16834: welding consumables - wire electrodes, wires, rods and deposits for gas shielded arc welding of high strength steels - Classification. 2012.
[51] ANSI/AWS D1.1/D1.1M. Structural Welding Code – Steel; 2015.
[52] EN 1011-2. Welding - recommendation for welding of metallic materials - Part 2: arc welding of ferritic steels. 2001.
[53] ISO 17642-3: destructive tests on welds in metallic materials - cold cracking tests for weldments - arc welding processes - Part 3: externally loaded tests. 2005.
[54] ANSI/AWS B4.0. Standard methods for mechanical testing of welds. 2016.
[55] Rhode M, Schaupp T, Muenster C, Mente T, Boellinghaus T, Kannengiesser T. Hydrogen determination in welded specimens by carrier gas hot extraction—a review on the main parameters and their effects on hydrogen measurement. Weld World 2019;63:511–26. https://doi.org/10.1007/s40194-018-0664-9.
[56] Rhode M. Hydrogen diffusion and effect on degradation in welded microstructures of creep-resistant low-alloyed steels. BAM-Dissertationsreihe; 2016. Band 148, https://nbn-resolving.org/urn:nbn:de:kobv:b43-374027.
[57] Salmi S, Rhode M, Jüttner S, Zinke M. Hydrogen determination in 22MnB5 steel grade by use of carrier gas hot extraction technique. Weld World 2015;59:137–44. https://doi.org/10.1007/s40194-014-0186-z.
[58] Malard B, Remy B, Scott C, Deschamps A, Chêne J, Dieudonné T, Mathon MH. Hydrogen trapping by VC precipitates and structural defects in a high strength Fe–Mn–C steel studied by small-angle neutron scattering. Mater Sci Eng A 2012;536:110–6. https://doi.org/10.1016/j.msea.2011.12.080.
[59] Valentini R, Solina A, Matera S, De Gregorio P. Influence of titanium and carbon contents on the hydrogen trapping of microalloyed steels. Metall Mater Trans 1996;27:3773–80. https://doi.org/10.1007/BF02595626.
[60] Van den Eeckhout E, De Baere I, Depover T, Verbeken K. The effect of a constant tensile load on the hydrogen diffusivity in dual phase steel by electrochemical permeation experiments. Mater Sci Eng A 2020;773:138872. https://doi.org/10.1016/j.msea.2019.138872.
[61] Dueren C. Formulae for calculating the maximum hardness in the heat-affected zone of welded joints. IIW-Doc 1986;IX:1437–86.
[62] Yurioka N, Okumura M, Kasuya T, Cotton H. Prediction of HAZ hardness of transformable steels. Met Constr-Brit Weld 1987;19:217R–23R.
[63] Zhang L, Kannengiesser T. HAZ softening in Nb-, Ti- and Ti + V-bearing quenched and tempered steel welds. Weld World 2016;60:177–84. https://doi.org/10.1007/s40194-016-0299-7.
[64] Spachinger SJ, Ernst W, Enzinger N. Influence of Ti on the toughness of the FGHAZ and the CGHAZ of high-strength microalloyed S700MC steels. Weld World 2017;61:1117–31. https://doi.org/10.1007/s40194-017-0480-7.
[65] Laureys A, Claeys L, De Seranno T, Depover T, Van den Eeckhout E, Petrov R, Verbeken K. The role of titanium and vanadium based precipitates on hydrogen induced degradation of ferritic materials. Mater Char 2018;144:22–34. https://doi.org/10.1016/j.matchar.2018.06.030.
[66] Merson ED, Myagkikh PN, Poluyanov VA, Merson DI, Vinogradov A. Quasi-cleavage hydrogen-assisted cracking path investigation by fractographic and side surface observations. Eng Fract Mech 2019;214:177–93. https://doi.org/10.1016/j.engfracmech.2019.04.042.
[67] Beachem CD. A new model for hydrogen-assisted cracking (hydrogen embrittlement). Metall Trans 1972;3:441–55. https://doi.org/10.1007/BF02642048.
[68] Gedeon SA, Eagar TW. Assessing hydrogen-assisted cracking fracture modes in high-strength steel weldments. Weld J 1990;69:213s–20s.
[69] Martin ML, Fenske JA, Liu GS, Sofronis P, Robertson IM. On the formation and nature of quasi-cleavage fracture surfaces in hydrogen embrittled steels. Acta Mater 2011;59:1601–6. https://doi.org/10.1016/j.actamat.2010.11.024.
[70] Martin ML, Robertson IM, Sofronis P. Interpreting hydrogen-induced fracture surfaces in terms of deformation processes: a new approach. Acta Mater 2011;59:3680–7. https://doi.org/10.1016/j.actamat.2011.03.002.
[71] Guedes D, Cupertino Malheiros L, Oudriss A, Cohendoz S, Bouhattate J, Creus J, Thébault F, Piette M, Feaugas X. The role of plasticity and hydrogen flux in the fracture of a tempered martensitic steel: a new design of mechanical test until fracture to separate the influence of mobile from deeply trapped hydrogen. Acta Mater 2020;186:133–48. https://doi.org/10.1016/j.actamat.2019.12.045.
[72] ISO 18265. Conversion of hardness values; 2003.